




# Direct numerical simulation of a supersonic turbulent boundary layer over a compression–decompression corner

Cite as: Phys. Fluids **33**, 065111 (2021); <https://doi.org/10.1063/5.0052453>

Submitted: 31 March 2021 • Accepted: 17 May 2021 • Published Online: 07 June 2021

 Junyi Duan (段俊亦),  Xin Li (李欣),  Xinliang Li (李新亮), et al.

## COLLECTIONS

Paper published as part of the special topic on [Selected Papers from the 11th National Congress on Fluid Mechanics of China](#)



[View Online](#)



[Export Citation](#)



[CrossMark](#)

## ARTICLES YOU MAY BE INTERESTED IN

[Improvement of the free-interaction theory for shock wave/turbulent boundary layer interactions](#)

Physics of Fluids **33**, 075104 (2021); <https://doi.org/10.1063/5.0050113>

[Direct numerical simulation of supersonic turbulent expansion corner with shock impingement](#)

Physics of Fluids **33**, 105104 (2021); <https://doi.org/10.1063/5.0064741>

[Shock and shear layer interactions in a confined supersonic cavity flow](#)

Physics of Fluids **33**, 066102 (2021); <https://doi.org/10.1063/5.0050822>

**APL Machine Learning**

Open, quality research for the networking communities

**Now Open for Submissions**

[LEARN MORE](#)



# Direct numerical simulation of a supersonic turbulent boundary layer over a compression–decompression corner

Cite as: Phys. Fluids **33**, 065111 (2021); doi: 10.1063/5.0052453

Submitted: 31 March 2021 · Accepted: 17 May 2021 ·

Published Online: 7 June 2021



View Online



Export Citation



CrossMark

Junyi Duan (段俊亦),<sup>1,2</sup> Xin Li (李欣),<sup>3</sup> Xinliang Li (李新亮),<sup>1,2</sup> and Hongwei Liu (刘洪伟)<sup>1,a)</sup>

## AFFILIATIONS

<sup>1</sup>LHD, Institute of Mechanics, Chinese Academy of Sciences, Beijing 100190, China

<sup>2</sup>School of Engineering Science, University of Chinese Academy of Sciences, Beijing 100049, China

<sup>3</sup>Shanghai Electromechanical Engineering Institute, Shanghai 201109, China

**Note:** This paper is part of the special topic, Selected Papers from the 11th National Congress on Fluid Mechanics of China.

<sup>a)</sup>Author to whom correspondence should be addressed: [hliu@imech.ac.cn](mailto:hliu@imech.ac.cn)

## ABSTRACT

A direct numerical simulation of the interaction between a shock wave and the supersonic turbulent boundary layer in a compression–decompression corner with a fixed 24° deflection angle at Mach 2.9 is conducted. The characteristics of the shock interactions are investigated for two heights between the compression and decompression corners, corresponding to  $H/\delta_{ref} = 4.25, 1.22$ , where  $\delta_{ref}$  denotes the reference turbulent boundary layer thickness. A classic shock wave/turbulent boundary layer interaction flow is reproduced in the higher case. For the lower case, the size of the separation region is significantly decreased, and the low-frequency unsteadiness is slightly suppressed in the interaction region, as assessed by analyzing the mean and fluctuating wall pressure. Flow patterns near the reattachment line show the existence of the Görtler vortices. By analyzing the curvature radius and Görtler number distribution, it was found that a strong centrifuge instability is reserved in the compression corner region and reversed in the decompression corner region due to the convex streamline curvature. The downstream flow of the decompression corner is relatively complex where the additional shocklet and new stream-wise vortices are observed. A negative response mechanism is found regarding fluctuating wall-pressure signatures between the upstream and downstream of the decompression corner.

Published under an exclusive license by AIP Publishing. <https://doi.org/10.1063/5.0052453>

## I. INTRODUCTION

The problem of shock wave/turbulent boundary layer interactions (STBLIs) is frequently faced by high-speed aircraft, and it has a serious impact on aircraft layout and aerothermodynamic protection. The phenomena in interaction flows are very rich, including the unsteady motion of the shock system, the separation and reattachment of the turbulent boundary layer (TBL), and the breathing motion of the separation bubble. Ferri<sup>1</sup> first observed STBLIs when testing an airfoil in a high-speed wind tunnel. Great progress on this problem has been made through more than 70 years of exploration.<sup>2,3</sup> However, the current understanding of the complex flow mechanisms of low-frequency oscillations of shock waves and high heat flux in the reattachment region is insufficient, and in-depth study should be conducted.<sup>4</sup> A proper understanding of STBLIs will help develop the advanced hypersonic vehicles and provide a theoretical basis for engineering applications in aerospace contexts.

Besides the STBLI flows for extensively studied compression ramps, the supersonic turbulent flow over a compression–decompression corner (CC–DC) has also been observed frequently in high-speed aircraft, such as engine inlet, fore-body, and combustion chamber.<sup>5</sup> As shown in Fig. 1, the incoming TBL is disturbed by the interactions with the shock waves, expansion waves, and their combined effects. In the compression corner region, the TBL is decelerated and compressed under the strong adverse pressure gradient (APG), and the turbulence amplification occurs. In contrast, a supersonic turbulent boundary layer subjected to an expansion corner can undergo an acceleration and re-laminarization process.<sup>6,7</sup> The combined effects of turbulent amplification and re-laminarization in STBLI flows are still not fully understood, and the associated physical mechanisms need to be further investigated.

Grilli *et al.*<sup>8</sup> performed the first large eddy simulation (LES) study of the whole compression–decompression corner configuration with a deflection angle 25° at Mach 2.88, corresponding to experimental data

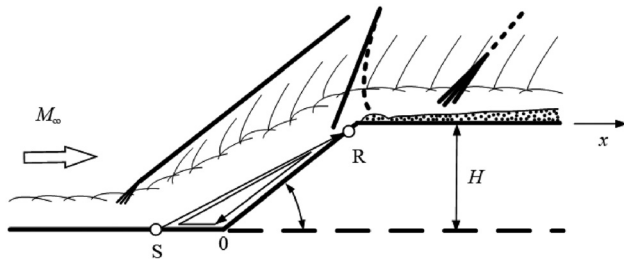


FIG. 1. A Sketch of compression–decompression STBLI flow.<sup>24</sup>

of Zheltovodov.<sup>9</sup> Their LES research reproduced kinds of typical experimental flow phenomena of STBLI, such as Görtler vortices and the unsteady nature of interaction region. Additional LES studies were carried out by Goshtasbi and Mousavi<sup>10</sup> in the same condition regarding geometry, boundary conditions, etc., as those used by Zheltovodov.<sup>9</sup> In their work, the influence of wall temperature, free-stream stagnation pressure, and Reynolds number on the shock behavior was investigated.

Over the past two decades, due to the rapid development of high-resolution and low-dissipation numerical algorithms and computation speed, the direct numerical simulation (DNS) method has been successfully applied to study STBLI flows and has gradually become an important tool in the flow mechanism investigations.<sup>11–17</sup> The first DNS study of compression ramp flow and oblique shock-wave/flat-plate boundary layer interaction flow were carried out by Admas<sup>11</sup> and Pirozzoli and Grasso,<sup>12</sup> respectively. Wu and Martin<sup>13</sup> also performed DNS studies on compression ramp flows with the incoming conditions similar to that of the wind tunnel experiments conducted by Bookey *et al.*,<sup>18</sup> where the agreement between numerical and experimental results has been achieved in terms of mean wall-pressure distribution, separation bubble length, and turbulent fluctuation amplification intensity. Meanwhile, the flow mechanism investigation was greatly promoted based on the high-fidelity DNS data. The shock wave low-frequency oscillation mechanism was analyzed by Martin's research group;<sup>15,19–21</sup> a new turbulence amplification mechanism was proposed by Fang *et al.*;<sup>17</sup> and turbulent kinetic energy transport mechanism was studied by Li *et al.*,<sup>14</sup> to name just a few.

Despite the classical compression ramp flows having been studied extensively, the DNS research of compression–decompression corner flow is still lacking. The DNS study of hypersonic TBL at Mach 6 over a compression/expansion corner was conducted by Ritos *et al.*<sup>22</sup> They mainly focused on the acoustic loading, i.e., pressure fluctuations beneath the interaction region. In their study, similarities and differences between hypersonic transitional boundary layer at Mach 7.2 with the compression/expansion corner flow, in the context of acoustic loading, have been drawn. In addition, DNS of STBLI in a compression–decompression corner flow was effectively carried out by a parallel algorithm proposed by Xu *et al.*<sup>23</sup> based on the architecture of multiple graphics processing units (GPU). Although various numerical studies of the compression–decompression corner flow have been performed, the shock interaction and expansion processes were usually analyzed separately; to our knowledge, the investigation of combined interactions involving TBL, shock wave, and expansion wave in the compression–decompression corner has not been reported.

In this paper, we perform a DNS study of supersonic Mach 2.9 turbulent boundary layer over a compression–decompression corner of a 24° deflection angle. The incoming flow conditions we use are similar to those in the experiments of Bookey *et al.*<sup>18</sup> and the DNS of Wu and Martin.<sup>13</sup> Two heights of the decompression corner (DC) are considered. The DNS data are validated against available experimental data and other DNS, and the detailed flowfield structures and turbulence statistics are analyzed to explore the essential flow phenomena taking place in the compression–decompression corner interaction configuration.

## II. COMPUTATIONAL SETUP AND VALIDATION

### A. Computational setup

The three-dimensional compressible Navier–Stokes (N–S) equations in curvilinear coordinates  $(\xi, \eta, \zeta)$  are solved numerically, written as follows:

$$\frac{\partial Q}{\partial t} + \frac{\partial(F + F_\nu)}{\partial \xi} + \frac{\partial(G + G_\nu)}{\partial \eta} + \frac{\partial(H + H_\nu)}{\partial \zeta} = 0, \quad (1)$$

where  $Q$  represents the conservative variables;  $F$ ,  $G$ , and  $H$  are the convective flux terms in the  $\xi$ ,  $\eta$ ,  $\zeta$  directions, respectively; and  $F_\nu$ ,  $G_\nu$ ,  $H_\nu$  are the corresponding viscous flux terms. The N–S equations are non-dimensionalized with unit reference length and freestream states, that is, velocity  $U_\infty$ , temperature  $T_\infty$ , density  $\rho_\infty$ , and dynamic viscosity  $\mu_\infty$ . The overall flowfield is a perfect gas, and Sutherland's law is used to calculate the viscosity coefficient. To close the N–S equations, the perfect gas state equation is enforced. More detailed formulas on the governing equation can be found in Tong *et al.*<sup>25</sup>

The DNS is performed by using a high-order finite difference code OpenCFD-SC developed by Li *et al.*,<sup>14,26</sup> and the governing equations are solved using the WENO-SYMO scheme,<sup>27</sup> with a combination of absolute and relative limiters,<sup>13</sup> and the Steger–Warming splitting approach for the discretization of the convective flux terms. An eighth-order central difference scheme is used to compute the viscous flux terms. For STBLI flows, high-order spatial discretization schemes are necessary to resolve much finer turbulence structures and capture the separation region accurately.<sup>28</sup> After all of the spatial terms are solved, the third-order Runge–Kutta method is used for time integration.

Steady laminar boundary layer profiles are imposed at the inlet; a buff region with a coarse mesh is put in place to eliminate the disturbance reflection in the outlet region, and the flow variables are obtained using two-order downstream extrapolation at the outlet. Nonreflecting boundary conditions are used at the top boundary, and periodic boundary conditions are used in the spanwise direction. A no-slip boundary condition is used, with constant wall temperature  $T_w = 307$  K ( $T_w/T_\infty = 2.84$ ) at the bottom wall. The fully developed incoming TBL is generated by the laminar-to-turbulent transition method used by Pirozzoli *et al.*<sup>29</sup> The same blowing and suction velocity disturbances are used to promote the transition in our DNS.

### B. Flow configuration

Two cases with vertical altitudes between the compression corner (CC) and DC of 28.47 mm (case A) and 8.13 mm (case B) are considered in this paper. Figure 2 gives a sketch of the computational domain and computational mesh. For both cases, the lengths of the upstream

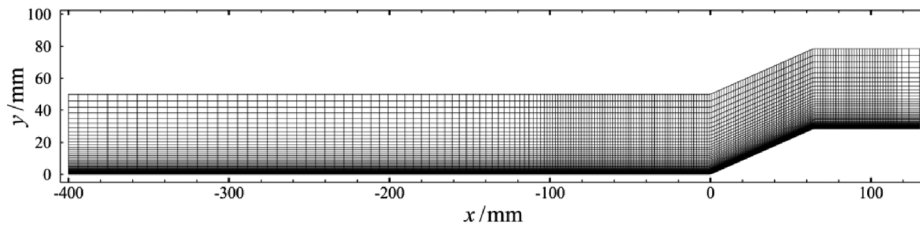


**FIG. 2.** Sketch of the computational mesh for case A. The mesh is plotted every 20 and 5 points in the  $x$  and  $y$  directions, respectively, for the convenience of visualization.

and downstream flat planes are 400 and 50 mm, respectively; the vertical distance  $L_y$  between the top and bottom boundary of the computational domain is 50 mm; and the spanwise length  $L_z$  is 28 mm.

As shown in Fig. 2, the mesh has straight and perpendicular lines in the  $x$  and  $y$  directions, except for in the near-wall region, where the grid orthogonality method is applied to achieve the normal mesh lines perpendicular to the wall surface. In the  $x$  direction, the mesh is smoothly adjusted to enhance resolution before  $x = -100$  mm; in the  $y$  direction, the mesh is hyperbolically stretched to increase the resolution in the wall region; and in the  $z$  direction, the mesh is uniformly distributed. Detailed information on the meshes and domain sizes of two cases is given in Table I. For the incoming TBL, the mesh resolutions in the  $x$  and  $z$  directions are 3.75 and 4.2, respectively; in the  $y$  direction, they are 0.45 on the wall surface and 5.8 at the edge of boundary layer. As Poggie *et al.*<sup>30</sup> suggested, the DNS level has been met, and the meshes used in our computation are capable of catching refined structures in the TBL.

### C. Validation

Before displaying and discussing the simulation results, the accuracy and reliability of the DNS data should be validated. In this section, two groups of flowfield properties, namely, the incoming TBL and the interaction region, are compared to available DNS data or experimental data. In the following analyses, the Reynolds average and density-weighted average for the general variable  $\phi$  are defined as  $\phi = \bar{\phi} + \phi'$  and  $\phi = \tilde{\phi} + \phi''$ , respectively, where  $\tilde{\phi} = \bar{\rho}\phi/\bar{\rho}$ . Note that the over bar denotes the average in the spanwise and timewise directions.

We first define the reference location at  $x/\delta_{ref} = -9$ , following Wu and Martin.<sup>13</sup> Here,  $\delta_{ref}$  denotes the thickness of the TBL at the reference location. Figures 3(a) and 3(b) show the van Driest transformed and original mean velocity profiles at the reference station, respectively, and Figs. 3(c) and 3(d) show the mean root square profile of the velocity fluctuation at the reference location. Agreement with the DNS data of Wu and Martin<sup>13</sup> and the experimental data of Bookey *et al.*<sup>18</sup>—which fall under similar incoming conditions—the compressible TBL DNS data of Pirozzoli *et al.*,<sup>12</sup> and the incompressible TBL DNS data of Wu and Moin<sup>31</sup> are shown in Fig. 3 and prove that the simulation of the undisturbed TBL region is credible. The properties of the incoming TBL, including the boundary layer

thickness  $\delta$ ; displacement thickness  $\delta^*$ ; momentum thickness  $\theta$ ; Mach number  $Ma$ ; momentum Reynolds number  $Re_\theta = \rho_\infty u_\infty \theta / \mu_\infty$ ; wall-skin friction coefficient  $C_f = \tau_w / 0.5 \rho_\infty U_\infty^2$ , where  $\tau_w$  denotes the wall shear stress, and incoming flow condition, containing density  $\rho_\infty$ ; streamwise velocity  $U_\infty$ ; temperature  $T_\infty$ , are collected in Table II and compared to the result of Wu and Martin<sup>13</sup> and Bookey *et al.*<sup>18</sup>

The power spectral density (PSD) is estimated by applying Welch's method with a Hamming window on the wall-pressure signal, which is decomposed into twelve segments with 50% overlaps. Note that PSD is a function of  $\omega$ , where  $\omega = 2\pi f$  is the angular frequency. The PSD function at the reference location, normalized by wall friction  $\tau_w$  and viscous time units  $\nu/u_\tau^2$ , is reported in Fig. 4. A good coincidence with the experimental data of Gravante *et al.*<sup>32</sup> and Farabee and Casarella<sup>33</sup> is achieved in the high-frequency end of the spectrum, which is dominated by the influence of near-wall motions.<sup>34</sup> This demonstrates that the collected wall-property signals have sufficient time resolution, and it further supports the reliability of our DNS results in compressible TBL.

The distributions of the wall-skin friction  $C_f$  and the wall-pressure  $p_w$  compared to DNS and experimental data of Wu and Martin<sup>13</sup> and Bookey *et al.*<sup>18</sup> are shown in Fig. 5. We observe that the distribution of  $C_f$  between case A and the previous DNS results collapsed in the region of incoming TBL, the separation region, the reattached boundary layer, and the separation point, as well as the reattachment point. In addition, the distribution of  $p_w$  between case A and the previous DNS results is very close, both within 5% of experimental error. In summary, the well-studied compression ramp flow is reproduced precisely in our compression–decompression corner flow (case A), verifying the reliability of the results in the interaction region.

## III. RESULTS AND DISCUSSION

### A. Mean and instantaneous flowfield

The mean wall-skin friction  $C_f$  and wall-pressure  $p_w$  are described above and are discussed in greater detail in this section. The mean skin-friction exhibits typical behavior for a separated flow. The length of the separation region, defined as  $L_{sep} = x_r - x_s$ , shrinks obviously in case B relative to case A. The separation point and the reattachment point displace about  $0.4 \delta_{ref}$  in the downstream direction and  $0.27 \delta_{ref}$  upstream. In Fig. 5(a), three extreme points are shown in the separation region, i.e., two minimal points and one maximal point (with the exception of a maximal point located at  $x = 0$ , the result of the discontinuity of the curvature of the wall's surface), which is associated with the breathing motion of the separation bubble, as suggested by Priebe and Martin.<sup>15</sup> The same can also be seen for case B, representing a similarity motion of the separation bubble.

In Fig. 5(b), the mean wall pressure, normalized by the pressure of the freestream, is constantly increased during the shock interaction

**TABLE I.** Computation domain size and mesh resolution.

	$Nx \times Ny \times Nz$	$H$ (mm)	$\Delta x^+$ , $(\Delta y_w^+, \Delta y_e^+)$ , $\Delta z^+$
Case A	$4000 \times 256 \times 300$	28.47	3.75, (0.45, 5.8), 4.2
Case B	$3400 \times 256 \times 300$	8.13	



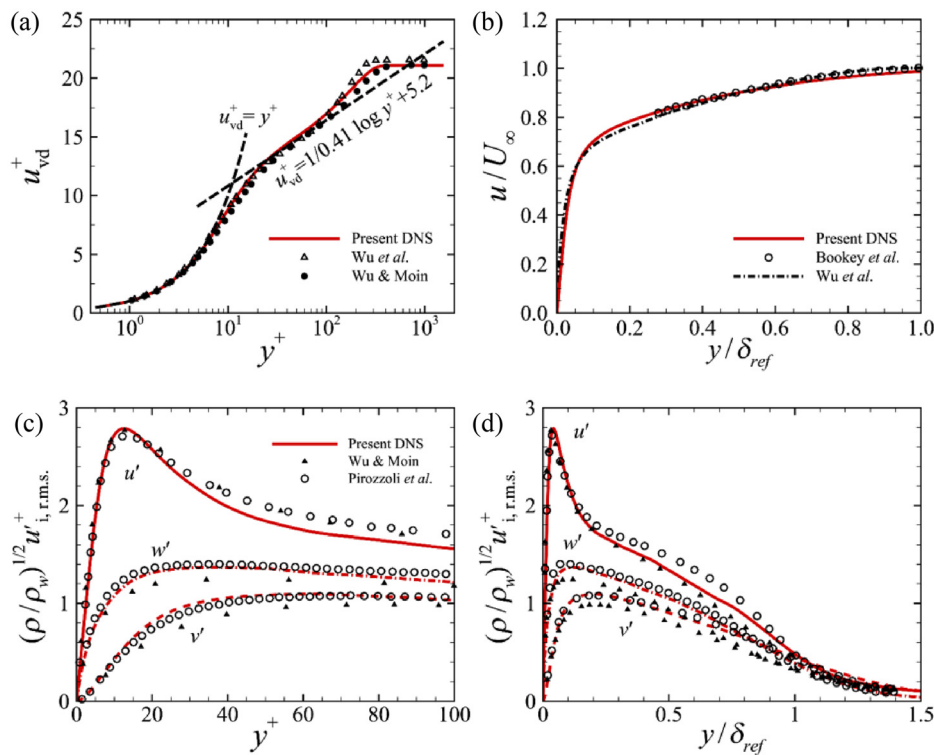


FIG. 3. Mean velocity profile at reference location in inner scaling (a) and outer scaling (b). Root mean square velocity fluctuation intensities at the reference location in inner scaling (c) and outer scaling (d).

TABLE II. Conditions for the incoming turbulent boundary layer.

	Ma	$Re_\theta$	$\theta$ (mm)	$\delta^*$ (mm)	$C_f$	$\delta$ (mm)	$\rho_\infty$ (kg/m <sup>3</sup> )	$U_\infty$ (m/s)	$T_\infty$ (K)
DNS <sup>13</sup>	2.9	2300	0.38	1.80	0.002 17	6.4	0.077	609.1	107.1
Experiment <sup>18</sup>	2.9	2400	0.43	2.36	0.002 25	6.7	0.074	604.5	108.1
Present DNS	2.9	2216	0.40	1.97	0.002 29	6.7	0.074	604.5	108.1

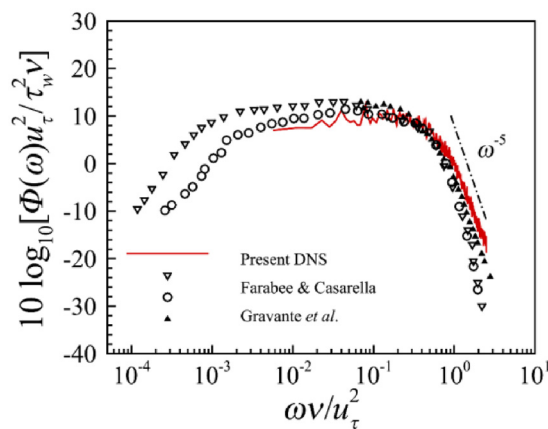


FIG. 4. Power spectral density of the wall-pressure at the reference location, normalized by inner time units and wall friction.

with a plateau inside the separation zone. It is interesting to note that the wall pressure increases slightly, within  $0.5\delta_{ref}$  downstream of DC for case B before dropping later to the initial values. The above distribution may imply that the compression wave or shocklet is generated downstream of expansion fan.

In the remainder of this section, the instantaneous flow structures are analyzed. The variable  $DSM$  is defined as follows:

$$DSM = 0.8 \exp[-10(x - x_{min})/(x_{max} - x_{min})], \quad (2)$$

where  $x = |\nabla \rho|$ . This is suggested by Wu and Martin<sup>13</sup> for plotting a numerical Schlieren plot. The instantaneous contour plots for  $DSM$  and an illustration of primary flow structures, including a  $\lambda$ -shock system, expansion waves, and separation bubbles, are presented in Fig. 6. Note that the range of axes used in case A and case B exhibit a relatively significant difference. For the compression–decompression corner flow, the incoming TBL is subject to interactions with shock waves and the expansion fan, and ultimately recovers its equilibrium state downstream. The entirety of this process is shown in Fig. 6(a), and

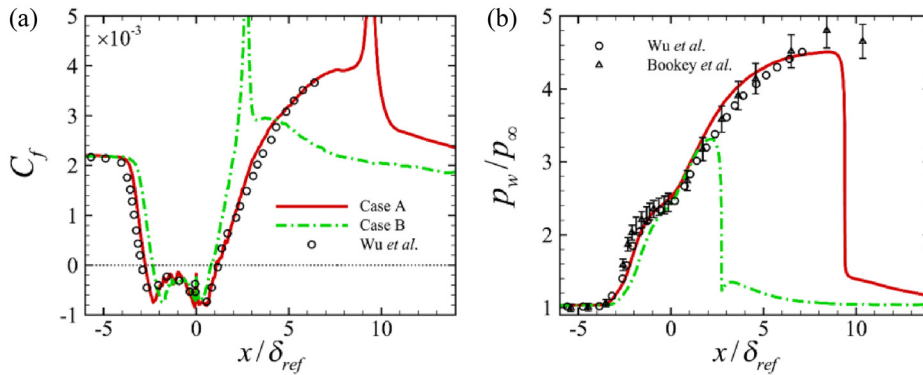


FIG. 5. Streamwise distributions of wall-skin friction (a) and wall-pressure (b).

additional interactions between the expansion waves and the reattached boundary layer are present, with respect to the compression ramp flow.

First, the typical  $\lambda$ -shock system generally observed in the Mach 2.9  $24^\circ$  compression ramp flows appears in the compression–decompression corner (case A). However, in Fig. 6(b), it is difficult to distinguish the first portion of the main shock, that is, the angle between them decreases acutely. The inviscid shock angle decreased from  $43^\circ$  in case A to  $34^\circ$  in case B. In contrast, the separation shock in case A results from the turning of the flow at the separation bubble upstream of the corner at  $29^\circ$ , which agrees accurately with Wu and Martin,<sup>13</sup> increased to  $31^\circ$  in case B.

In Fig. 6, a large-area sub-sonic region is seen downstream from the separation region, and the sonic lines are immediately close to the downstream flat plane under acceleration by the expansion fan. Another obvious phenomenon in Fig. 6(a) is that the height of coherent structures, located downstream of the DC, is greatly increased, compared to the upstream TBL and reattached boundary layer. In addition, a sharp shock can be seen in Fig. 6(b), located downstream from the expansion fan, compressing the over-expansion flow to match downstream backpressure.

The turbulent coherent vortex structures are visualized using the  $Q$  criterion.<sup>35</sup> The iso-surfaces of  $Q = 1\%Q_{max}$  are colored with local streamwise vorticity, with pressure gradient indicated with gray and that of  $u_s = 0$  given in black are shown in Fig. 7. This shows that organized, streamwise-elongated hair-pin vortices occur intermittently in the upstream TBL, which is consistent with the findings of Priebe *et al.*<sup>15</sup> and Fang *et al.*<sup>36</sup> Carefully comparing

the downstream recovery boundary layer with the upstream TBL in Fig. 7(b) indicates that many large-scale vortex structures are preserved from the upstream reattachment region and are broken down into small-scale streamwise vortex structures at a further downstream location. By contrast, these vortex structures occur only sparsely along the DC in case A, which is similar to the findings of Fang *et al.*<sup>36</sup> and Teramoto *et al.*,<sup>7</sup> which is in the supersonic expansion-corner flow. The classic streaky structures from the supersonic TBL are suppressed dramatically by expansion waves after they pass through the DC.

Streamwise velocity fluctuations contour map along the  $x$ – $z$  plane, located in linear-layer  $y^+ = 10$  and log-layer  $y^+ = 60$ , are plotted in Fig. 8. At the near-wall region, we observe the classic streamwise elongated streaks that occur upstream from the undisturbed TBL, and the spanwise distance between two neighboring low-speed streaks is about  $\Delta z^+ = 90 - 110$ . In the separation region and the upstream region of the DC, large-scale streaky structures with a spanwise length of about  $1\delta_{ref}$  can be observed in Fig. 8(a), indicating that the spanwise scale of the velocity fluctuations increased after they passed through the shock interaction region. Downstream of the DC, large-scale structures evolve rapidly into elongated streaks running streamwise, with a wider spanwise length than the upstream TBL, and they break down into small-scale structures of about  $2\delta_{ref}$ , which promote near-wall turbulence recovery toward the equilibrium state. However, at the log-layer, we observe that the difference in turbulence structures between those upstream and downstream of DC is much smaller in Fig. 8(b) with respect to the near-wall region.

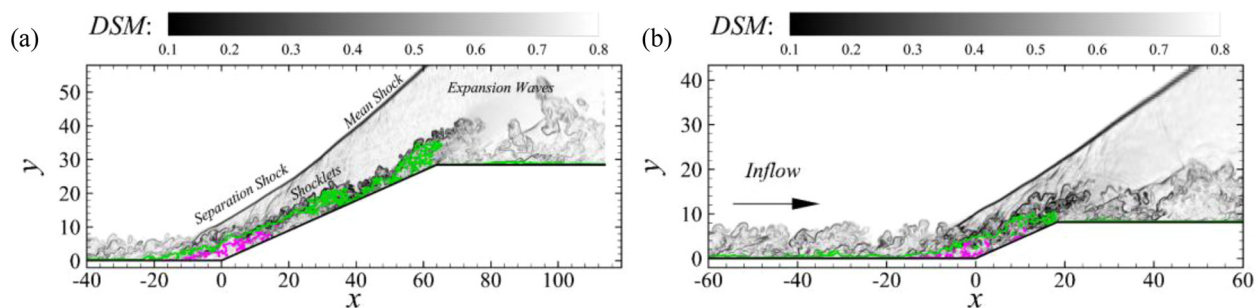
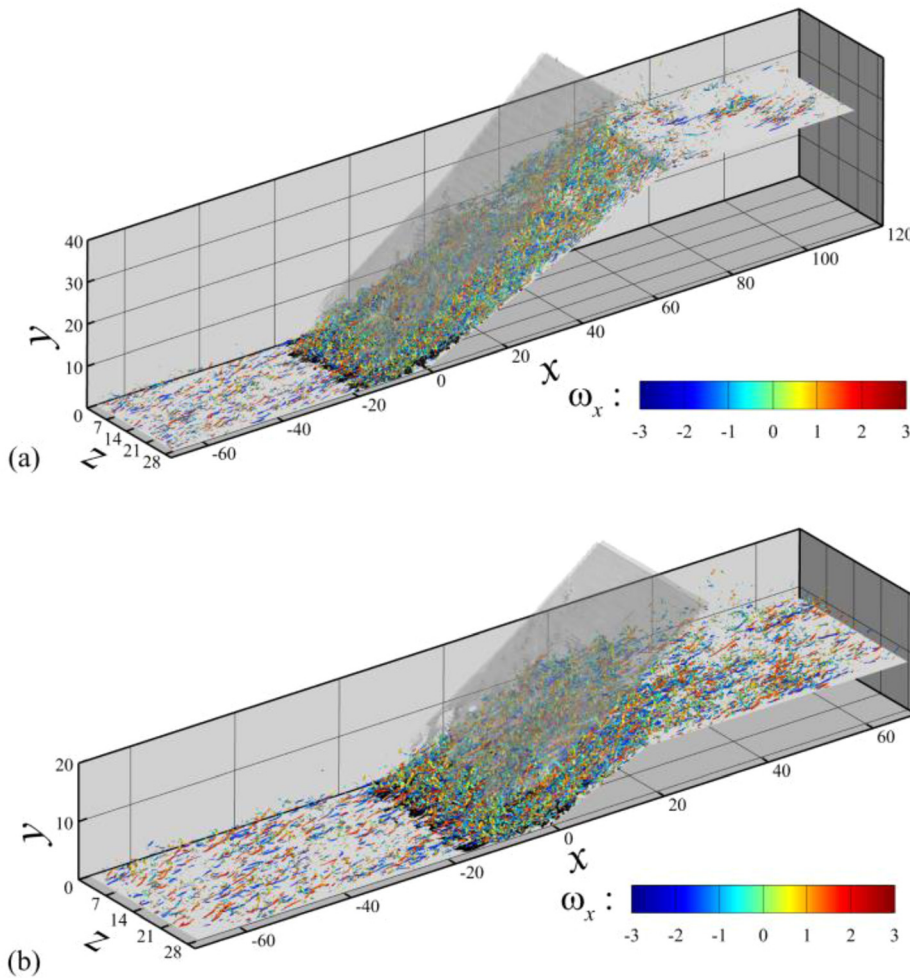


FIG. 6. Instantaneous numerical density schlieren for (a) case A and (b) case B. The pink line denotes the iso-line of  $u_s = 0$ ; and the green line denotes the sonic line.



**FIG. 7.** Turbulence coherent vortex structures in (a) case A and (b) case B visualized with the iso-surface of  $Q = 1\%Q_{max}$ , colored with the streamwise vorticity. The shock wave system is visualized with the iso-surface of pressure gradient, colored in gray. The recirculation region is visualized with the iso-surface of  $u_s = 0$ , colored in black.

## B. Görtler vortices

As indicated by Zheltovodov,<sup>37</sup> Görtler vortices are essential and important phenomena for compression–decompression corner flows. These structures arise from the instability of boundary layers with sufficiently concave streamwise curvatures, where the interaction among the centrifugal force, pressure gradient, and viscosity destabilizes the boundary layer, and the streamwise vortices, termed the Görtler vortices, arises as a consequence.<sup>38</sup> In 1940, Görtler showed that a centrifugal instability could occur in boundary layers over curved walls.<sup>39</sup> Although Görtler vortices were first detected in laminar flow, the same mechanism of instability also occurs in turbulent flows. A number of experimental observations<sup>5,40,41</sup> and numerical simulations<sup>5,8,21</sup> have reported these large-scale streamwise elongated vortices structures in compression ramp flows. The existence of Görtler vortices in an incident shock wave configuration has also been confirmed experimentally.<sup>42</sup> It may be that Görtler vortices are responsible for the amplification of turbulent fluctuations in the reattachment region, as well as associated with shock wave low-frequency oscillations.<sup>17,21</sup>

The Görtler number  $G_T$  can be used to estimate the generation of the Görtler instability in compressible turbulent flows. As Smits and

Dussauge<sup>43</sup> suggested, the Görtler number  $G_T$  can be defined as follows:

$$G_T = \frac{(\theta/\delta)^{\frac{3}{2}}}{0.018(\delta^*/\delta)} \sqrt{\frac{\delta}{R}}, \quad (3)$$

where the curvature radius  $R$  can be calculated via the mean velocity,

$$R = \frac{(u^2 + v^2)^{3/2}}{\left[ u^2 \frac{\partial v}{\partial x} - v^2 \frac{\partial u}{\partial y} + uv \left( \frac{\partial v}{\partial y} - \frac{\partial u}{\partial x} \right) \right]}, \quad (4)$$

and the curvature parameter  $\delta/R$  is defined as the ratio of the boundary layer thickness  $\delta$  to the curvature radius  $R$  of the streamline.

The distribution of the curvature parameter  $\delta/R$  and the Görtler number  $G_T$  along the two mean flow streamlines 1 passing through  $x/\delta_{ref} = -9.0$  and  $y/\delta_{ref} = 0.2$ , and 2, passing through  $x/\delta_{ref} = -9.0$  and  $y/\delta_{ref} = 0.6$ , is plotted in Fig. 9. For both two cases,  $\delta/R$  and  $G_T$  reach a peak value near the separation point, an observation that is consistent with Priebe *et al.*<sup>21</sup> and is much higher than the critical value of  $\delta/R = 0.03$  given by Smits and Dussauge<sup>43</sup> for Mach 3

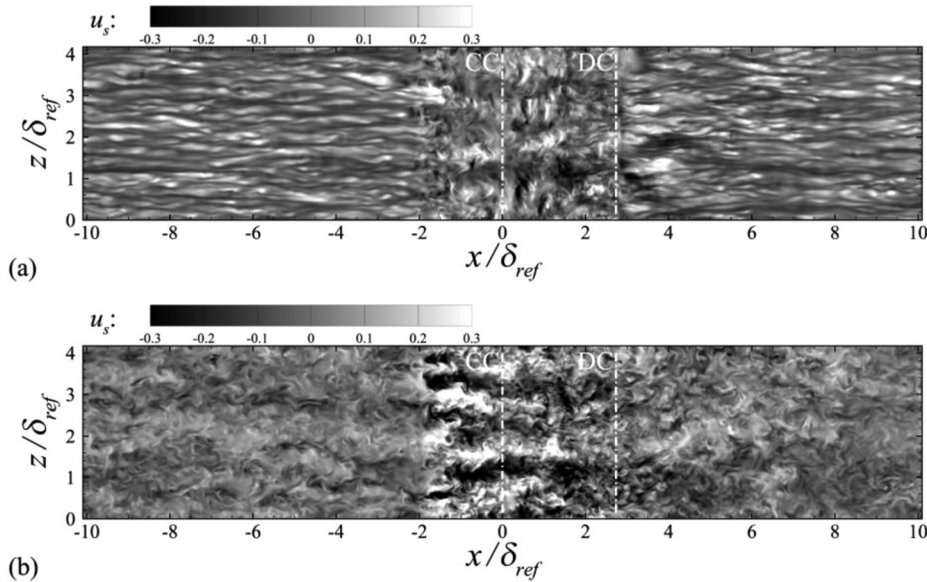


FIG. 8. Streamwise velocity fluctuation  $u'_s$  at (a)  $y^+ = 10$  and (b)  $y^+ = 60$  for case B.

flow and of  $G_T = 0.6$  given by Loginov *et al.*<sup>5</sup> for laminar flows. Although no specifically critical value for turbulent flow has been determined, it is reasonable to conjecture that centrifugal instability mechanisms are likely part of the explanation for the observed streamwise vortices in corner flows. We found that the distributions of the curvature parameter  $\delta/R$  and the Görtler number  $G_T$  are very similar near the separation point and in the reattachment region in the two cases, revealing the flow similarity between case A and case B in the region of shock interaction.

The time-averaged streamwise vorticity component  $\omega^*$  in the  $y$ - $z$  plane is presented in Figs. 10–12 to better describe the flow within the boundary layer. Note that level  $\omega^* = 0$  is deleted to ensure that image remains comprehensible, and  $\omega^*$  is transformed into the direction parallel to the wall surface, defined as follows:

$$\begin{aligned}\omega^* &= \omega_x \cos \alpha + \omega_y \sin \alpha, \\ \omega_x &= (\partial w / \partial y - \partial v / \partial z) \delta_{ref} / U_\infty, \\ \omega_y &= (\partial u / \partial z - \partial w / \partial x) \delta_{ref} / U_\infty,\end{aligned}\quad (5)$$

where  $\omega_x$  and  $\omega_y$  are, respectively, the horizontal and vertical time-averaged vorticity components in the Cartesian coordinates  $(x, y, z)$ .  $\alpha$  is the angle between wall surface and horizontal direction. Two locations are considered in this paper, E1 ( $x^* = -1.0$ ) and E2 ( $x^* = 0.5$ ) with transformed coordinates via the following formula:  $x^* = (x - x_{DC}) / \delta_{ref}$ , where  $x_{DC}$  denotes the location of DC.

For both cases, the distribution of vorticity  $\omega^*$ , located upstream of DC (E1), is shown in Fig. 10. Counter-rotating vortices can clearly be seen. The localized regions within the TBL, with alternately appearing positive and negative vortices, can be observed. The distance between the neighboring positive (negative) regions is about  $\Delta z = 2\delta_{ref}$ . In general, this further confirms the Görtler-like vortices generated in our compression–decompression corner flow, regardless of the interaction with the downstream expansion fan. With the exception of the intense vorticity region within the boundary layer, we also

found an intense region located at  $y/\delta_{ref} < 0.1$ , with the same alternate pattern, probably the result of high shear, caused by the wall-bounded decelerating effect.

The distribution of vorticity  $\omega^*$ , located downstream of DC (E2), is shown in Fig. 11. Compared to the upstream distribution (E1), we found that large-scale roll cells disappear, but near-wall high-vorticity regions are reserved during the expansion process. That is to say, the strength of upstream Görtler vortices is suppressed when they pass through the expansion fan due to the bulk dilation effect. It is interesting to note in Fig. 12 that new vortices occur in the near-wall high-vorticity region  $y^+ < 30$ , with an opposite rotation direction from the Görtler vortices. The cores of such vortex structures reside at  $y^+ = 11$ , and the spanwise width on inner scales is about  $z^+ = 260$ . To our knowledge, the observation as well as generation of such new streamwise vortices has not been reported in DNS for compression–decompression corner flows.

Figures 13 and 14 show the time-averaged streamwise skin-friction  $C_{fx}$  and spanwise skin-friction  $C_{fz}$  on the wall surface, calculated via the following formulas:

$$C_{fx} = \frac{\mu_w \frac{\partial \langle u_s \rangle}{\partial y_n} \Big|_{\text{wall}}}{\frac{1}{2} \rho_\infty U_\infty^2} \quad \text{and} \quad C_{fz} = \frac{\mu_w \frac{\partial \langle w \rangle}{\partial y_n} \Big|_{\text{wall}}}{\frac{1}{2} \rho_\infty U_\infty^2}, \quad (6)$$

where  $\langle u_s \rangle$  and  $\langle w \rangle$  denote the time-averaged velocity parallel to the wall surface and spanwise direction, respectively.  $y_n$  is the wall normal direction,  $\mu_w$  is the wall dynamic viscosity, and  $\rho_\infty$  and  $U_\infty$  are the density and velocity of the freestream, respectively. At the beginning of the separation region, we observe that the distributions of  $C_{fx}$  are mainly two-dimensional, and the vectors are parallel to the streamwise direction. However, in the reattachment region of case A, three-dimensional characteristics can be seen in Fig. 13(a), and the downstream pink line has an approximative sinusoidal waveform shape along the spanwise direction, with a wavelength of about  $2 \delta_{ref}$ . This



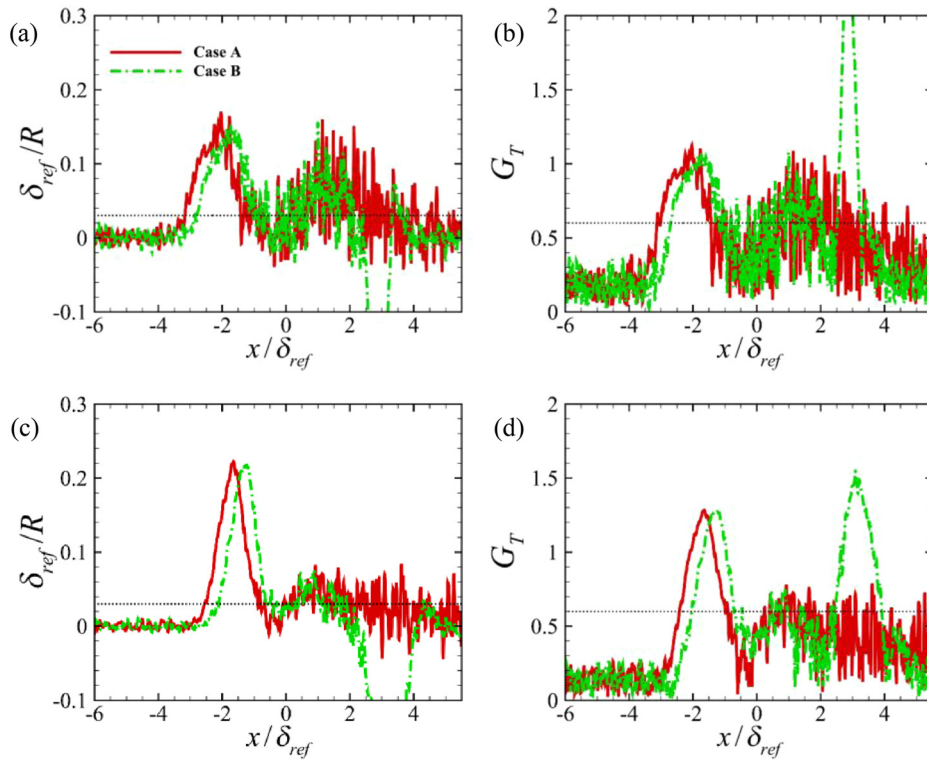


**FIG. 9.** Streamline curvature parameter  $\delta_{ref}/R$  and Görtler number  $G_T$  along two mean flow streamlines: [(a) and (b)] streamline 1 passing through  $x/\delta_{ref} = -9.0$  and  $y/\delta_{ref} = 0.2$ , [(c) and (d)] streamline 2 passing through  $x/\delta_{ref} = -9.0$  and  $y/\delta_{ref} = 0.6$ .

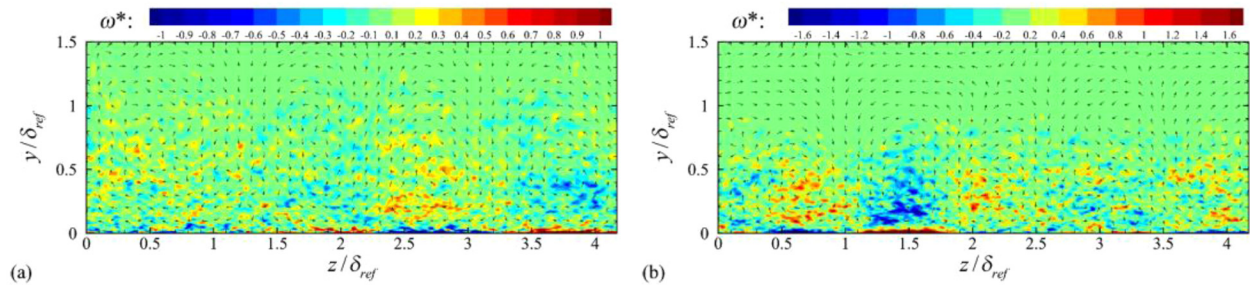


**FIG. 10.** Time-averaged streamwise vorticity  $\omega^*$  and velocity vectors in  $y$ - $z$  planes at  $x^* = -1.0$  for (a) case A and (b) case B.

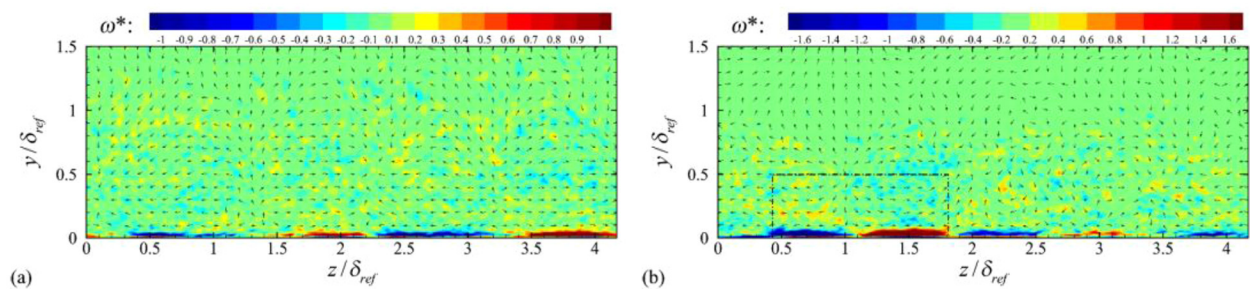


**FIG. 11.** Time-averaged streamwise vorticity  $\omega^*$  and velocity vectors in  $y$ - $z$  planes at  $x^* = 0.5$  for (a) case A and (b) case B.

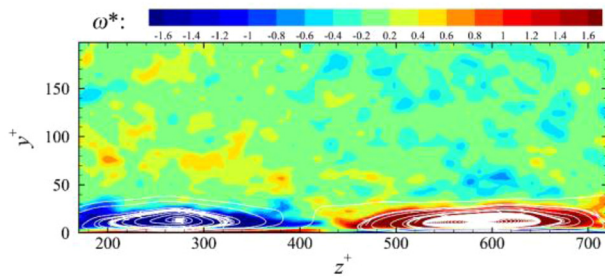


**FIG. 12.** Magnified view of black dashed box in Fig. 11(b) on inner scales. The white curves denote the streamlines in  $y$ - $z$  plane.

phenomenon is also found in the earlier research<sup>5,8</sup> on STBLI flows, such as in the compression–decompression corner, the compression ramp, or the incident shock configurations, and it is widely considered to occur in the presence of Görtler vortex structures, which promote

the upwash of lower momentum fluids and downwash of higher momentum fluids, as shown in Fig. 10, leading to skin-friction uneven distributions in the spanwise direction, this is consistent with the finding in Ref. 44.

Unlike case A, the distribution of  $C_{fx}$  in Fig. 13(b) reflects only one pair of Görtler vortices, reserved in the range of  $3\text{ mm} < z < 17\text{ mm}$ . In the remainder of the range, the pink lines are roughly parallel to the spanwise direction, indicating an absence of Görtler vortices. In the vicinity of the reattachment, the uneven spanwise distributions of  $C_{fx}$  can also be found downstream of DC, with an opposite trend to the upstream region in both cases. Additional details on the relationship of turbulent fluctuations between the upstream and downstream DC are given in Sec. III D.

The distribution for the time-averaged spanwise skin-friction  $C_{fz}$ , superimposed by four spanwise locations named S1 to S4, is plotted in Fig. 14. Note that the values of  $C_{fz}$  in the regions of the oblique ramp (between the black dashed-dotted lines) and slightly downstream of DC are much greater than those in the TBL, where  $C_{fz}$  is

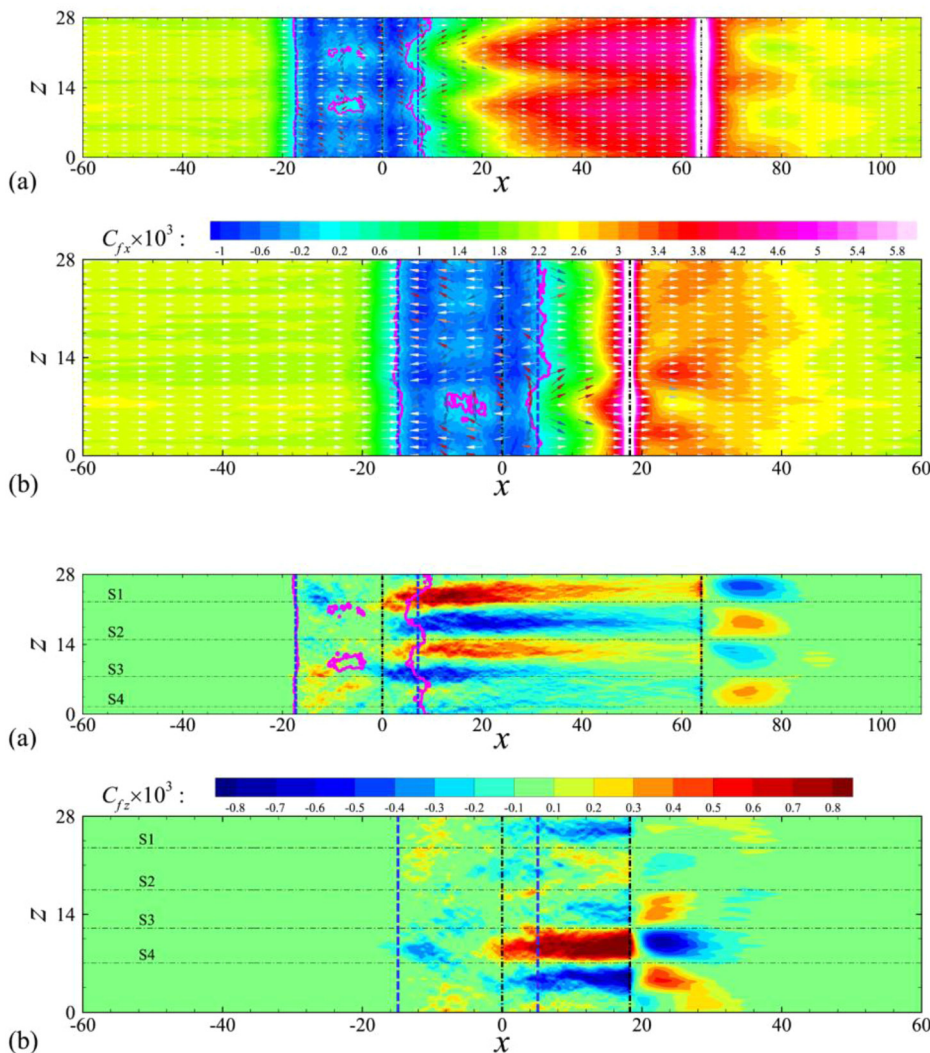


**FIG. 13.** Time-averaged streamwise skin-friction coefficient  $C_{fx}$  and skin-friction vectors map for (a) case A and (b) case B. The pink solid and blue dashed lines denote the iso-lines of time-averaged and time-spanwise averaged  $C_{fx} = 0$ , respectively. The vectors are obtained by streamwise and spanwise wall shear stress and colored according to the angle between them. The black lines denote the position of compression–decompression corner.

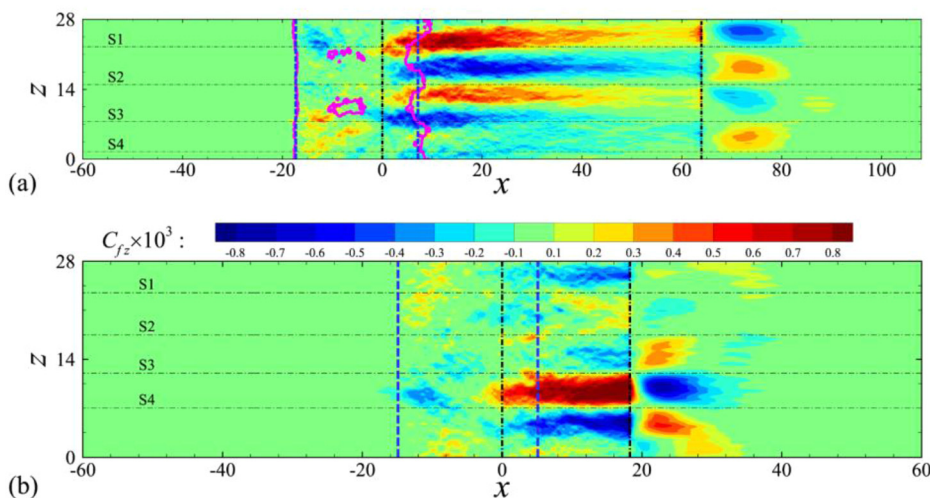


**FIG. 14.** Time-averaged spanwise skin-friction coefficient  $C_{fz}$  for (a) case A and (b) case B.



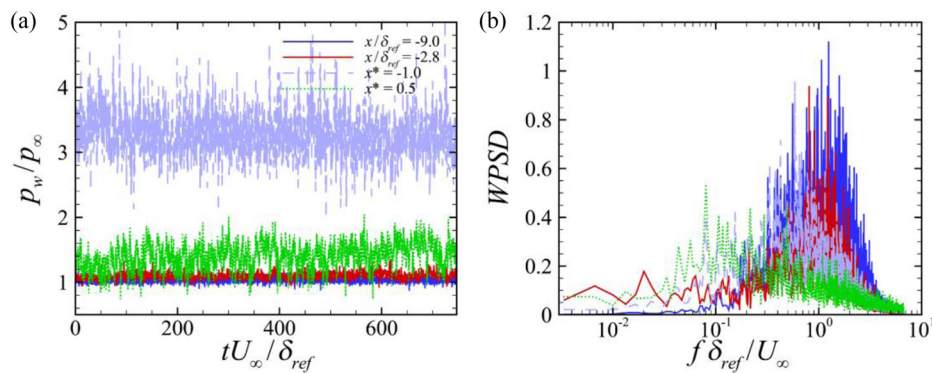


FIG. 15. Wall-pressure signals (a) and corresponding weighted power spectral density (b) at different streamwise locations.

approximately equal to zero. In addition, patterns with alternating positive and negative values can be observed in the oblique ramp regions in Fig. 14, which represents the footprint of the Görtler vortices. This implies that such structures tend to find stable spanwise locations; otherwise, time-averaged  $C_{fz}$  should be around zero, resembling the behavior of TBL. This is consistent with the experimental observation of Görtler vortices, visualized by oil flow. The distribution of  $C_{fz}$  downstream from DC also represents the footprint of the new backwards-rotate streamwise vortices and further confirms the occurrence of such structures. In addition, the survival region is up to  $2.3 \delta_{ref}$  for case A, and  $1.4 \delta_{ref}$  for case B downstream of DC. About the effect of those vortices on the statistics of flowfield, we think it may be relatively weak. There are probably two reasons: first, the flow characteristics are dominated by the effect of bulk dilation, and the turbulent fluctuations are greatly weakened during passing through the decompression corner; second, the strength and size of those vortices is weak and small. The influenced region is very limited.

The DNS result for the compression–decompression corner flow (case A) reproduces some primary aspects of STBLI flows, including the  $\lambda$ -shock system, mean wall-property distribution, and Görtler vortices. In the remainder of the paper, we analyze case B and provide its detailed flow statistics and turbulent structures.

### C. Wall-pressure signature and frequency spectrum

When an incoming TBL is disturbed by the shock wave or a Prandtl–Meyer expansion wave, the statistics and spectrum characteristics for turbulent fluctuations located in the nonequilibrium interaction region are significantly affected.<sup>45–47</sup> To present the unsteady motion of the shock wave system and the unsteady features of the downstream flowfield, the wall-pressure signals at different streamwise locations are shown in Fig. 15(a). At  $x/\delta_{ref} = -9$ , the probe beneath the undisturbed TBL at the reference location, the signal oscillates around unity with slight fluctuations. Near the mean separation point  $x/\delta_{ref} = -2.8$ , the signal strolls between 1 and 1.3 are superimposed over high-frequency turbulent fluctuations. As pointed by Dolling and Or, the wall pressure signal under the moving shock wave structure is generated by the superposition of the shock-induced fluctuations on the undisturbed TBL signal. The pressure probe at  $x^* = -1.0$  (E1) is located in the reattachment region upstream of the DC. The wall-pressure level is increased to 3.3 due to the compression that takes place along the corner, and the level of fluctuations is increased dramatically, which corresponds to intense turbulence convected from

the detached shear layer. At the position  $x^* = 0.5$  (E2), which lies downstream of the DC, the mean wall-pressure value reduced to 1.35. In addition, the magnitude of fluctuations slightly increased with respect to the position  $x/\delta_{ref} = -9$ , and the relative intense fluctuations generated within the inner layer downstream from the DC can be confirmed.

The corresponding weighted power spectral density (WPSD) of wall-pressure signals is shown in Fig. 15(b). WPSD is calculated as follows:  $WPSD = f \cdot PSD / \int PSD df$ , where  $PSD$  is the power spectral density and calculated in the same way as the frequency spectrum shown in Fig. 4. The contour map of WPSD as a function of the dimensionless frequency  $St_\delta = f\delta_{ref}/U_\infty$  and the streamwise coordinate  $x/\delta_{ref}$  is also plotted in Fig. 16 to further illustrate the unsteady features of the entire interaction region. In Figs. 15(b) and 16, upstream of the shock-interaction region, such as the reference location  $x/\delta_{ref} = -9$ , the most energetic frequencies are located about  $St_\delta \approx 1.0$  which is a general feature of TBL. Note that near the mean separation point, highlighted by a black solid line in the figure, we can observe that the frequency  $St_\delta \approx 0.02$ , which is much lower than the energetic frequency of TBL  $St_\delta \approx 1.0$ , has much more energy compared with TBL. Although the energy of the low-frequency stage for case B is weaker than that of the conventional compression corner flows, it also reflects the low-frequency, unsteady nature of the shock system in our compression–decompression corner flow. The low-frequency unsteady motion of the shock wave is a typical feature for the STBLIs, and its cause remains an open question.<sup>2,49</sup>

As shown in Fig. 15(b), the energetic frequency of E2 distributes mainly in the middle-frequency band  $St_\delta \approx 0.1$ , which is greatly lower than that of E1. We found that at the downstream vicinity of DC, the

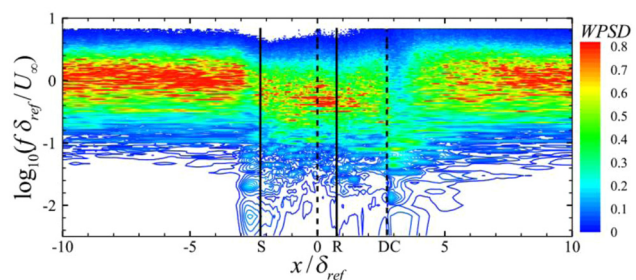
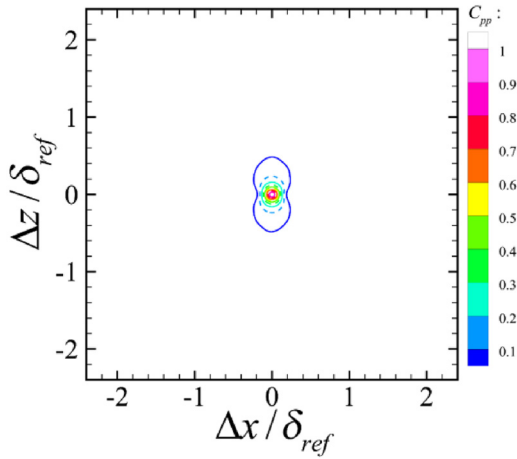


FIG. 16. Weighted power spectral density of wall-pressure fluctuation.



**FIG. 17.** Iso-lines of the two-point correlation  $C_{pp}$  in the  $x$ - $z$  plane at the reference location. Ten equally spaced contour levels are shown, from  $-0.1$  to  $0.9$  (the zero iso-line is omitted).

overall distribution of energy tends to a lower frequency in Fig. 16. Most energy is more uniformly distributed around  $St_\delta \approx 0.03 - 0.3$ , which is consistent with the LES result of Grilli *et al.*<sup>8</sup> for the compression–decompression corner configuration. In general, this indicates that the flow characteristics at the downstream vicinity of DC are dominated by large-scale structures.

#### D. Statistical characteristics of turbulence fluctuations

To assess the spatial characteristics of the nonequilibrium fluctuating flowfield disturbed by shock waves and by Prandtl–Meyer expansion waves, two-point correlation analyses are conducted at various streamwise locations. The definition employed by Bernardini *et al.*<sup>45</sup> is also used in this study, defined as follows:

$$C_{pp}(x; \Delta x, \Delta z) = \frac{p'(x, 0, z, t)p'(x + \Delta x, 0, z + \Delta z, t)}{p'_{r.m.s}(x)p'_{r.m.s}(x + \Delta x)}, \quad (7)$$

where  $\Delta x$  and  $\Delta z$  represent the streamwise and spanwise spatial separations, respectively, and  $x$  is the streamwise target coordinate.

A two-point correlation map for wall-pressure fluctuations at the reference location is given in Fig. 17. As shown in previous research on wall-pressure fluctuations in an incompressible or compressible TBL,<sup>32,45,46,50,51</sup> the iso-lines of  $C_{pp}$  are roughly circular at small separations, indicating an isotropic state of small-scale pressure fluctuations. At large separations, the iso-lines become elongated in the spanwise direction, representing a weakly anisotropic nature of the large-scale structures.<sup>45</sup> Our simulation results for TBL are consistent with the above experimental or DNS data.

The characteristic fluctuating wall-pressure length scales are increased in both directions, as indicated in Fig. 18. This shows that the dumbbell-shaped iso-lines take on an elliptic shape upstream of DC, indicating greater elongation in the streamwise direction. Downstream of DC, the shapes of the iso-lines at large separations are completely destroyed under the strong interaction of the expansion fan. In general, the characteristic distributions of  $C_{pp}$  can be divided into four distinct sub-zones. Note that the occurrence of three pieces of sub-zones with a negative two-point correlation up to  $-0.2$  ranged along the positive one can be seen in Figs. 18(b) and 18(c). For vertical negative cores, this further confirms that large-scale streamwise vortices exist on a spanwise scale of  $2\delta_{ref}$ . This may also be associated with shocklets or compression waves that are generated intermittently in the spanwise direction downstream of DC. More evidence is needed to support this hypothesis. In addition, the connection between the downstream and the upstream of turbulent fluctuations is cutoff by the DC, and the upstream part of the regions is transformed into a negative sub-zone. The same situation can be observed in the vertical adjacent regions. Analyses of wall-pressure signatures reveal the occurrence of a negative corresponding mechanism to the compression–decompression corner conjugation for wall-pressure fluctuations between the upstream and downstream of DC.

The probability density functions (PDFs) of the wall-pressure fluctuations are normalized by their local root mean square (rms), following Dolling and Or,<sup>48</sup> at various spatial locations that are shown in Fig. 19. The standard normal distribution is also given, for reference. In Fig. 19(a), it is obvious that the PDFs are highly skewed and have a positive skewness coefficient about  $0.4$ – $0.75$ , regardless of their spanwise locations upstream of DC. The flatness coefficients at E1 are around  $4.4$ , much greater than that of the standard normal distribution, indicating that the Görtler vortices have a relative effect on intensifying the intermittent of signatures at reattachment region.

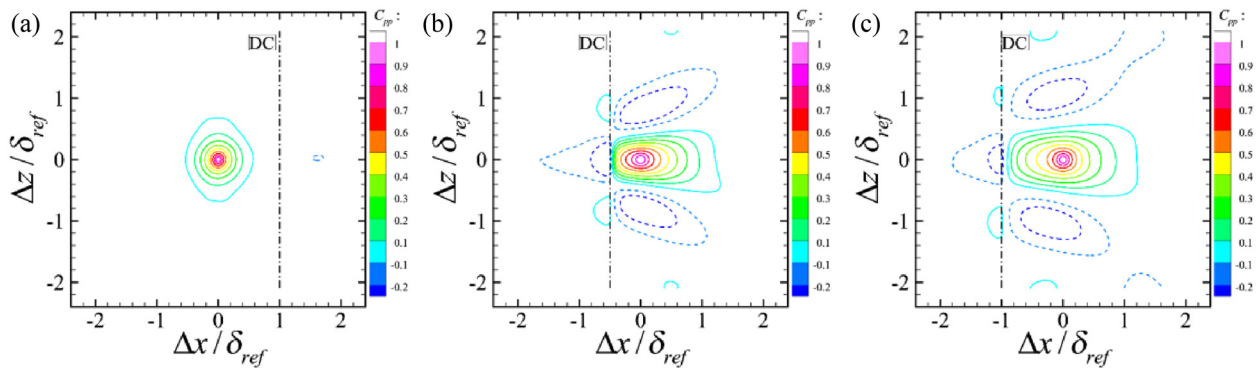


**FIG. 18.** Iso-lines of the two-point correlation  $C_{pp}$  in  $x$ - $z$  plane at  $x^* = -1.0, 0.5, 1.0$  in (a)–(c). The negative iso-lines and position of DC are highlighted by dash lines and black dash dot line, respectively. Note that iso-lines equal to  $-0.1$  and  $-0.2$  are added (compare to Fig. 17).



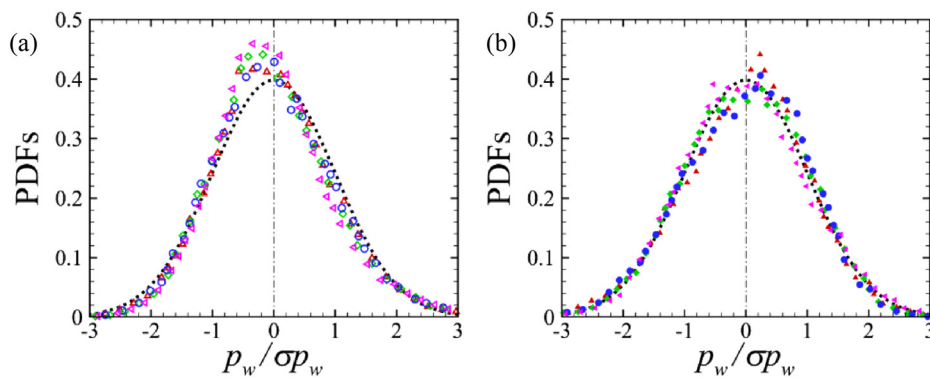


FIG. 19. PDFs for the wall-pressure fluctuations at (a) E1 and (b) E2. The red delta, green diamond, blue circle, and pink left triangle represent S1, S2, S3, and S4, respectively.

Downstream of DC, the distribution of the PDFs becomes more symmetrical, but a weak skew can be observed in Fig. 20(b), with an inverse skewness coefficient of about  $-0.17$  against upstream distribution except S4. Further evidence is provided to support the so-called negative corresponding mechanism mentioned above. Additionally, the flatness coefficients at E2 are around 2.9, which are quite close to that of the standard normal distribution, reflecting the weakness on large-scale turbulent fluctuations during the expansion process.

The overall sound pressure level (SPL) is a representative quantity used to assess acoustic loading. It can be obtained by transforming the pressure fluctuations,  $\text{SPL} = 20 \log_{10}(p'_{\text{rms}}/p_0)$  dB, where  $p_0 = 20 \mu\text{Pa}$ . Drawing on the distribution of SPL given in Fig. 20, it is found that the intense-loading areas are largely reattached boundary layers and mean shock wave regions, which agrees well with the numerical study in the compression–decompression corner by Ritos *et al.*<sup>22</sup> It is interesting to note a relatively intense loading region originates from the DC point, and this is highlighted by the green line, indicating the occurrence of shocklets or compression waves. Therefore, pressure fluctuations suffer the series intensification–relaxation–intensification when passing through the DC, and they ultimately recover to the same level of TBL.

In Fig. 21, the instantaneous pressure gradients at four spanwise locations are shown to indicate the tiny shocklet structures located downstream of DC. For better visualization, a set of relatively high contour levels is selected to reduce the number of compression waves detected within the boundary layer. The occurrence of intense compression in the separated shear layer and the shock wave can be seen

in Fig. 21, and the number of shocklets located in the narrow area between shock wave and shear layer also can be observed.

Shocklets radiating from the DC occur simultaneously in the S1 and S3 planes, corresponding to a region of high-level fluctuation intensity shown in Fig. 20. These unexpected structures are separated by a spanwise distance of about  $2 \delta_{\text{ref}}$  consistent with upstream incoming Görtler vortices, which may be due to the high-speed flow downwash, also caused by Görtler vortices, before it passes through the DC. In addition, the structures are responsible for a negative two-point correlation in the spanwise direction (Fig. 18), and the low-frequency energy increased in the weighted PSD map (Fig. 16). Small-scale streamwise vortex structures located close to the wall downstream of the DC can be actuated due to the spanwise pressure gradient.

#### IV. CONCLUSIONS

In this paper, a DNS study of a Mach 2.9 STBLI flow in the  $24^\circ$  compression–decompression corner was carried out. Vertical altitudes  $H/\delta_{\text{ref}}$  equal to 4.25 and 1.22 between the CC and the DC were considered. For the greater case, the statistics of the wall properties (i.e., mean pressure distribution, skin-friction distribution, and skin-friction vectors), the  $\lambda$ -shock system, and Görtler vortices are the same as those for the typical compression ramp flow. In the shorter case, a smaller separation bubble and slightly higher-frequency shock motion is found. Further, the centrifuge instability mechanism within the shock interaction region is completely reserved, resulting in the generation of Görtler vortices and three-dimensional characteristics in the

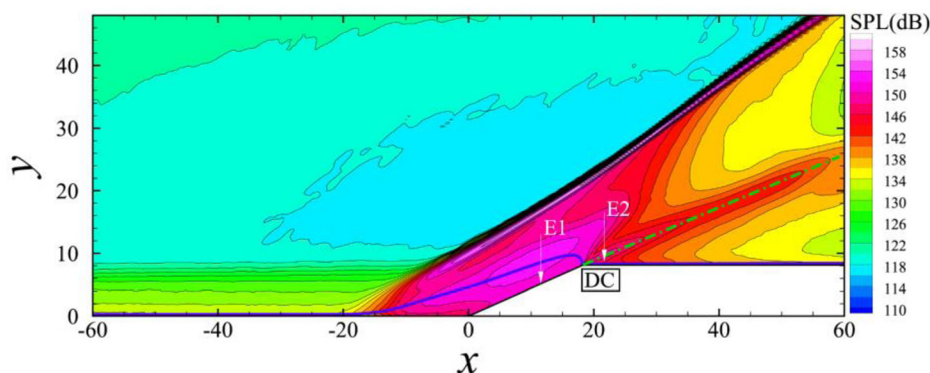


FIG. 20. Contour plot for sound pressure levels for case B. Blue line denotes mean sonic line.

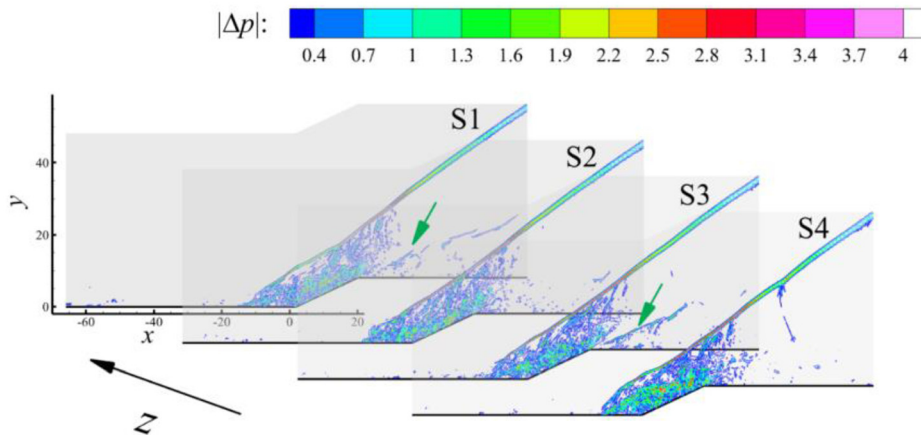


FIG. 21. Instantaneous pressure gradient modulus at four different spanwise locations (S1–S4).

downstream attachment region, whereas a convex streamline curvature through the expansion fan as well as bulk dilatation effect at the DC dramatically weakened those large-scale vortices.

In the shorter case, the additional shocklet structures, closely connected with upstream Görtler vortices were found downstream of the expansion fan. PSD analyses indicate the low-frequency nature of such structures, much lower than the energetic frequency in TBL. In addition, an intermittent distribution of the shocklets along the spanwise direction can also be observed. Therefore, newer streamwise vortex pairs were promoted by the spanwise differential pressure.

PDF and two-point correlation analyses revealed a negative signal responding mechanism occurring in the downstream portion of compression–decompression corner flows although the detailed dynamics principle between upstream and downstream turbulence of DC requires further investigations. Conducting further in-depth research of this kind would be worthwhile.

## ACKNOWLEDGMENTS

This work was supported by the National Key Research and Development Program of China (Nos. 2019YFA0405300 and 2016YFA0401200) and NSFC Projects (No. 91852203), National Numerical Windtunnel project, Science Challenge Project (No. TZ2016001), and Strategic Priority Research Program of Chinese Academy of Sciences (No. XDC01000000).

The authors thank the National Supercomputer Center in Tianjin (NSCC-TJ) for providing computing resources.

## DATA AVAILABILITY

The data that support the findings of this study are available from the corresponding author upon reasonable request.

## REFERENCES

- A. Ferri, "Experimental results with airfoils tested in the high-speed tunnel at Guidonia," Report No. 946 (1940).
- N. T. Clemens and V. Narayanaswamy, "Low-frequency unsteadiness of shock wave/turbulent boundary layer interactions," *Annu. Rev. Fluid Mech.* **46**, 469 (2014).
- D. V. Gaitonde, "Progress in shock wave/boundary layer interactions," *Prog. Aerosp. Sci.* **72**, 80 (2015).
- D. S. Dolling, "Fifty years of shock-wave/boundary-layer interaction research: What next?," *AIAA J.* **39**, 1517 (2001).
- M. S. Loginov, N. A. Adams, and A. A. Zheltovodov, "Large-eddy simulation of shock-wave/turbulent-boundary-layer interaction," *J. Fluid Mech.* **565**, 135 (2006).
- R. Narasimha and K. R. Sreenivasan, "Relaminarization in highly accelerated turbulent boundary layers," *J. Fluid Mech.* **61**, 417 (1973).
- S. Teramoto, H. Sanada, and K. Okamoto, "Dilatation effect in relaminarization of an accelerating supersonic turbulent boundary layer," *AIAA J.* **55**, 1469 (2017).
- M. Grilli, S. Hickel, and N. A. Adams, "Large-eddy simulation of a supersonic turbulent boundary layer over a compression–expansion ramp," *Int. J. Heat Fluid Flow* **42**, 79 (2013).
- A. A. Zheltovodov, V. M. Trofimov, E. Schüle, and V. N. Yakovlev, "An experimental documentation of supersonic turbulent flows in the vicinity of forward- and backward-facing ramps," Report No. 2030 (Institute of Theoretical and Applied Mechanics, USSR Academy of Sciences, Novosibirsk, 1990).
- E. Goshtasbi Rad and S. M. Mousavi, "Wall modeled large eddy simulation of supersonic flow physics over compression-expansion ramp," *Acta Astron.* **117**, 197 (2015).
- N. A. Adams, "Direct simulation of the turbulent boundary layer along a compression ramp at  $M=3$  and  $Re(\theta)=1685$ ," *J. Fluid Mech.* **420**, 47 (2000).
- S. Pirozzoli and F. Grasso, "Direct numerical simulation of impinging shock wave/turbulent boundary layer interaction at  $M=2.25$ ," *Phys. Fluids* **18**, 065113 (2006).
- M. Wu and M. P. Martín, "Direct numerical simulation of supersonic turbulent boundary layer over a compression ramp," *AIAA J.* **45**, 879 (2007).
- X. Li, D. Fu, Y. Ma, and X. Liang, "Direct numerical simulation of shock/turbulent boundary layer interaction in a supersonic compression ramp," *Sci. China Phys., Mech. Astron.* **53**, 1651 (2010).
- S. Priebe and M. P. Martín, "Low-frequency unsteadiness in shock wave-turbulent boundary layer interaction," *J. Fluid Mech.* **699**, 1 (2012).
- F. Tong, C. Yu, Z. Tang, and X. Li, "Numerical studies of shock wave interactions with a supersonic turbulent boundary layer in compression corner: Turning angle effects," *Comput. Fluids* **149**, 56 (2017).
- J. Fang, A. A. Zheltovodov, Y. Yao, C. Moulinec, and D. R. Emerson, "On the turbulence amplification in shock-wave/turbulent boundary layer interaction," *J. Fluid Mech.* **897**, A32 (2020).
- P. Booke, C. Wyckham, A. Smits, and M. P. Martín, "New experimental data of STBLI at DNS/LES accessible Reynolds numbers," in *43rd AIAA Aerospace Sciences Meeting and Exhibit* (American Institute of Aeronautics and Astronautics, Reno, Nevada, 2005).
- M. Wu and M. P. Martín, "Analysis of shock motion in shockwave and turbulent boundary layer interaction using direct numerical simulation data," *J. Fluid Mech.* **594**, 71 (2008).

- <sup>20</sup>S. Priebe, M. Wu, and M. P. Martín, "Direct numerical simulation of a reflected-shock-wave/turbulent-boundary-layer interaction," *AIAA J.* **47**, 1173 (2009).
- <sup>21</sup>S. Priebe, J. H. Tu, C. W. Rowley, and M. P. Martín, "Low-frequency dynamics in a shock-induced separated flow," *J. Fluid Mech.* **807**, 441 (2016).
- <sup>22</sup>K. Ritos, D. Drikakis, I. W. Kokkinakis, and S. M. Spottswood, "Computational aeroacoustics beneath high speed transitional and turbulent boundary layers," *Comput. Fluids* **203**, 104520 (2020).
- <sup>23</sup>D. Xu, S. Luo, J. Song, J. Liu, and W. Cao, "Direct numerical simulations of supersonic compression-expansion slope with a multi-GPU parallel algorithm," *Acta Astron.* **179**, 20 (2021).
- <sup>24</sup>H. Babinsky and J. K. Harvey, *Shock Wave-Boundary-Layer Interactions* (Cambridge University Press, 2011).
- <sup>25</sup>F. Tong, X. Li, Y. Duan, and C. Yu, "Direct numerical simulation of supersonic turbulent boundary layer subjected to a curved compression ramp," *Phys. Fluids* **29**, 125101 (2017).
- <sup>26</sup>X. L. Li, D. X. Fu, Y. W. Ma, and X. Liang, "Direct numerical simulation of compressible turbulent flows," *Acta Mech. Sin./Lixue Xuebao* **26**, 795 (2010).
- <sup>27</sup>M. P. Martín, E. M. Taylor, M. Wu, and V. G. Weirs, "A bandwidth-optimized WENO scheme for the effective direct numerical simulation of compressible turbulence," *J. Comput. Phys.* **220**, 270 (2006).
- <sup>28</sup>I. W. Kokkinakis, D. Drikakis, K. Ritos, and S. M. Spottswood, "Direct numerical simulation of supersonic flow and acoustics over a compression ramp," *Phys. Fluids* **32**, 066107 (2020).
- <sup>29</sup>S. Pirozzoli, F. Grasso, and T. B. Gatski, "Direct numerical simulation and analysis of a spatially evolving supersonic turbulent boundary layer at  $M = 2.25$ ," *Phys. Fluids* **16**, 530 (2004).
- <sup>30</sup>J. Poggie, N. J. Bisek, and R. Gosse, "Resolution effects in compressible, turbulent boundary layer simulations," *Comput. Fluids* **120**, 57 (2015).
- <sup>31</sup>X. Wu and P. Moin, "Direct numerical simulation of turbulence in a nominally zero-pressure-gradient flat-plate boundary layer," *J. Fluid Mech.* **630**, 5 (2009).
- <sup>32</sup>S. P. Gravante, A. M. Naguib, C. E. Wark, and H. M. Nagib, "Characterization of the pressure fluctuations under a fully developed turbulent boundary layer," *AIAA J.* **36**, 1808 (1998).
- <sup>33</sup>T. M. Farabee and M. J. Casarella, "Spectral features of wall pressure fluctuations beneath turbulent boundary layers," *Phys. Fluids A* **3**, 2410 (1991).
- <sup>34</sup>W. K. Blake, *Mechanics of Flow-Induced Sound and Vibration* (Academic Press, 1986).
- <sup>35</sup>J. Jeong and F. Hussain, "On the identification of a vortex," *J. Fluid Mech.* **285**, 69 (1995).
- <sup>36</sup>J. Fang, Y. Yao, A. A. Zheltovodov, Z. Li, and L. Lu, "Direct numerical simulation of supersonic turbulent flows around a tandem expansion-compression corner," *Phys. Fluids* **27**, 125104 (2015).
- <sup>37</sup>A. A. Zheltovodov, "Peculiarities of development and modeling possibilities of supersonic turbulent separated flows," Separated Flows and Jets: IUTAM Symposium (1991), Vol. 225.
- <sup>38</sup>J. M. Floryan, "On the Görtler instability of boundary layers," *Prog. Aerosp. Sci.* **28**, 235 (1991).
- <sup>39</sup>H. Görtler, "Instabilität laminarer Grenzschichten an konkaven wänden gegenüber gewissen dreidimensionalen Störungen," Report No. 1375 (1954).
- <sup>40</sup>J. Ginoux, "Experimental evidence of three-dimensional perturbations in the reattachment of a two-dimensional laminar boundary layer at  $M = 2.05$ ," Technical Report TCEA TN1 Rhode-Saint-Genese, Belgium, 1958. (TCEA TN1 Training Center for Experimental Aerodynamics, Rhode-Saint-Genese, Belgium, 1958).
- <sup>41</sup>M. S. Selig, J. Andreopoulos, K. C. Muck, J. P. Dussauge, and A. J. Smits, "Turbulence structure in a shock wave/turbulent boundary-layer interaction," *AIAA J.* **27**, 862 (1989).
- <sup>42</sup>Y. Zhuang, H. J. Tan, X. Li, F. J. Sheng, and Y. C. Zhang, "Letter: Görtler-like vortices in an impinging shock wave/turbulent boundary layer interaction flow," *Phys. Fluids* **30**, 061702 (2018).
- <sup>43</sup>A. J. Smits and J. P. Dussauge, *Turbulent Shear Layers in Supersonic Flow*, 2nd ed. (Springer, NY, 2006).
- <sup>44</sup>S. Cao, I. Klioutchnikov, and H. Olivier, "Görtler vortices in hypersonic flow on compression ramps," *AIAA J.* **57**, 3874 (2019).
- <sup>45</sup>M. Bernardini, S. Pirozzoli, and F. Grasso, "The wall pressure signature of transonic shock/boundary layer interaction," *J. Fluid Mech.* **671**, 288 (2011).
- <sup>46</sup>Y. Na and P. Moin, "The structure of wall-pressure fluctuations in turbulent boundary layers with adverse pressure gradient and separation," *J. Fluid Mech.* **377**, 347 (1998).
- <sup>47</sup>S. Priebe and M. P. Martín, "Turbulence in a hypersonic compression ramp flow," *Phys. Rev. Fluids* **6**, 034601 (2021).
- <sup>48</sup>D. S. Dolling and C. T. Or, "Unsteadiness of the shock wave structure in attached and separated compression ramp flows," *Exp. Fluids* **3**, 24 (1985).
- <sup>49</sup>K. M. Porter and J. Poggie, "Selective upstream influence on the unsteadiness of a separated turbulent compression ramp flow," *Phys. Fluids* **31**, 016104 (2019).
- <sup>50</sup>H. Choi and P. Moin, "On the space-time characteristics of wall-pressure fluctuations," *Phys. Fluids A* **2**, 1450 (1990).
- <sup>51</sup>L. Duan, M. M. Choudhari, and M. Wu, "Numerical study of acoustic radiation due to a supersonic turbulent boundary layer," *J. Fluid Mech.* **746**, 165 (2014).